ACS APPLIED MATERIALS & INTERFACES

RESEARCH ARTICLE

www.acsami.org

Architecture-Dependent Surface Chemistry for Pt Monolayers on Carbon-Supported Au

Shuang Cheng,[†,‡] Robert E. Rettew,[†] Marc Sauerbrey,[†] and Faisal M. Alamgir*[,†]

[†]School of Materials Science and Engineering, Georgia Institute of Technology, Atlanta, Georgia 30332, United States

[‡]School of Physical Science and Technology, Lanzhou University, Lanzhou 730000, People's Republic of China

ABSTRACT: Pt monolayers were grown by surface-limited redox replacement (SLRR) on two types of Au nanostructures. The Au nanostructures were fabricated electrochemically on carbon fiber paper (CFP) by either potentiostatic deposition (PSD) or potential square wave deposition (PSWD). The morphology of the Au/CFP heterostructures, examined using scanning electron microscopy (SEM), was found to depend on the type of Au growth method employed. The properties of the Pt deposit, as studied using X-ray photoelectron spectroscopy (XPS), X-ray absorption spectroscopy (XAS), and cyclic voltammetry (CV), were found to depend strongly on the morphology of the support. Specifically, it was found that smaller Au morphologies led to a higher degree of cationicity in the resulting Pt deposit, with Pt^{4+} and Pt^{2+} species being identified using XPS and XAS. For fuel-cell catalysts, the resistance of ultrathin catalyst deposits to surface area loss through dissolution, poisoning, and agglomeration is critical. This study shows that an equivalent of two monolayers (ML) is the low-loading limit of Pt on Au. At 1 ML or below, the Pt film decreases in activity and durability very rapidly due to presence of cationic Pt.

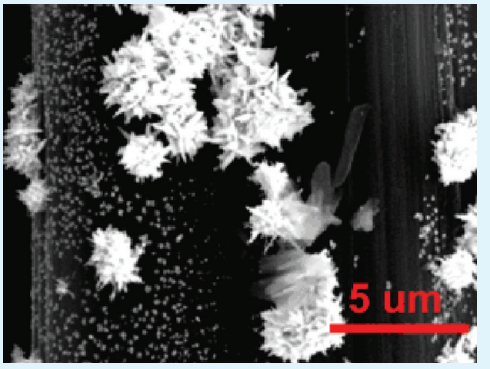

KEYWORDS: architecture Au, CFP, Pt, Cu UPD, methanol oxidation

INTRODUCTION

Direct methanol fuel cells (DMFCs) are currently the subject of extensive interest due to their promise as high efficiency power sources free of the problems of hydrogen storage and transport.[1−3] However, one of the limiting factors for DMFCs currently in development is the rate of methanol oxidation reaction (MOR) at the anode. Pt is currently the catalyst of choice for MOR in acidic media, although the two primary drawbacks of platinum, its high cost and low poisoning resistance, have yet to be completely mitigated. Therefore, one of the main goals of catalyst development for DMFCs is to modify the Pt catalyst in order to decrease its cost while increasing robustness and efficiency.[4−6] Surface area and electronic conductivity can be increased in order to achieve this goal.[7,8] Additionally, attempts have been made to decrease the amount of Pt required through the use of monolayer/submonolayer Pt catalyst films.[9,10] Finally, attempts to develop bimetallic Pt compounds in order to reduce Pt loading while increasing poisoning resistance have been reported for systems such as Pt−Ru[11,12] and Pt−Au.[1,13−15]

Methanol electro-oxidation, the reaction central to the direct methanol fuel cells (DMFCs), exhibits difficulties when performed on monometallic Pt catalysts because of poisoning effects caused by adsorption of intermediates such as carbon monoxide (CO) produced during the multistep reaction process. These surface poisons can be difficult to remove at low temperatures, leading to a catalyst surface that is inactive towards the MOR until specialized poison removal steps are undertaken. This phenomenon is one of the primary causes of performance loss from the Pt-catalyzed DMFC system. This problem has recently been addressed by the addition of an oxophilic metal alloyed with the Pt catalyst to enhance its CO tolerance. The increased tolerance is generally accepted to arise from the increased presence of OH^- groups on the alloy surface as compared that of the monometallic Pt surface, leading to a decrease in potential required to oxidatively remove CO from the surface. Ru is the most frequently employed oxophilic metal used in this role, but it suffers from poor electrochemical stability.[3,11] Recently, alloying of Pt with Au has been shown to be of interest due to the strong electronic interaction between Pt and Au and the possible slight expansion in the lattice parameter.[16] It is also well known that Au also has a stabilizing effect on Pt even under high oxidizing conditions and thus can suppress Pt dissolution during MOR, resulting in improved durability of the Pt−Au catalysts.[14,17] These properties have led to investigation into the catalytic activity of Pt upon Au-alloying, which may promote the methanol oxidation reaction (MOR).[1,18]

This paper focuses on determining the ultimate low-loading limit of Pt and the effect of the near-surface architecture on the electro-catalytic performance as dictated by the low-dimensional atomic/electronic structure of Pt atoms. We explore the effect of the Au−carbon fiber paper (CFP) morphology on the structural and chemical properties of Pt catalyst films and determining how

Received: June 27, 2011
Accepted: September 15, 2011
Published: September 15, 2011

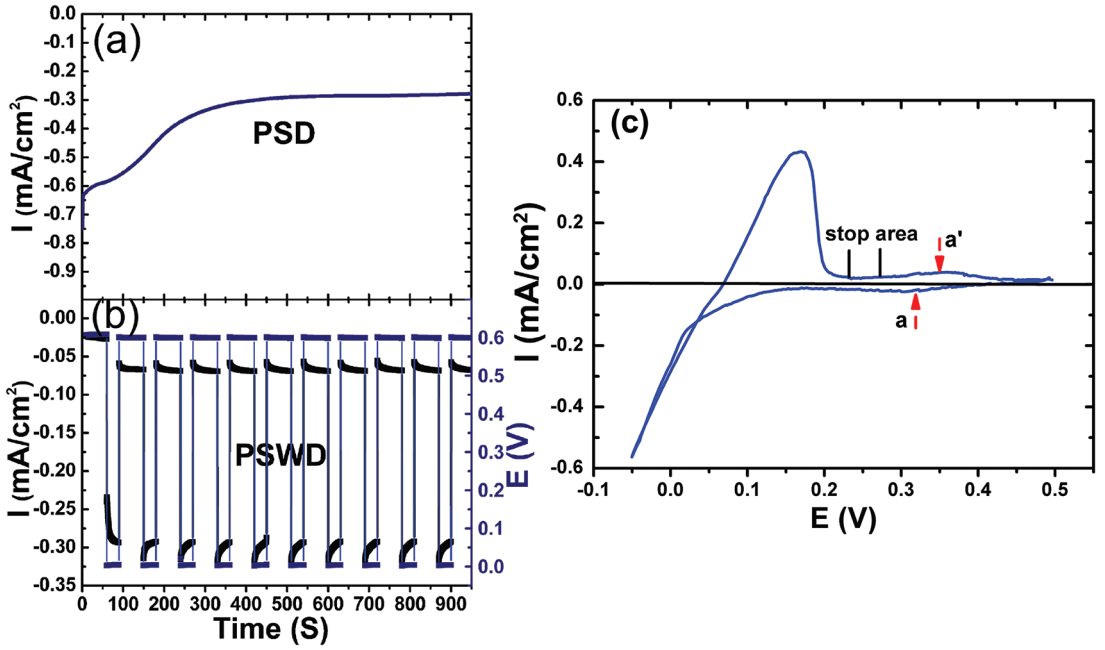

Figure 1. Voltage−time and current−time transients for fabrication of Au−CFP electrodes by (a) PSD and (b) PSWD methods. Typical Cu UPD voltammetry (c) employed for SLRR modification of Au−CFP with Pt.

changes in these properties influence the electrochemical performance and durability of the catalyst architecture as a whole.

In this study, the ultrathin platinum overlayers were prepared on two types of Au structures grown on CFP. A series of micro-scale Au nuclei were grown using potentiostatic deposition (PSD) for one series of samples, while the second series of samples, featuring nanoscale Au particles, employed potential square-wave deposition (PSWD). Layer-by-layer Pt growth on the Au−CFP surface was conducted by surface limited redox replacement (SLRR), by which Pt replacement of an underpotentially deposited (UPD) Cu adlayer resulted in a submonolayer-equivalent of deposited Pt. This growth method not only greatly reduces the Pt loading as compared to bulk potentiostatic or galvanostatic Pt growth but also provides high dispersion of Pt which is very critical to obtaining high electroactivity and power density for DMFC systems. SLRR is a very versatile technique in that it can be performed with a variety of different metals as sacrificial layers, including UPD Pb or overpotentially grown Ni.[9,19,20] For this work, the authors have elected to employ Cu UPD to fabricate the sacrificial layer, as it is less toxic than Pb and has also been more widely employed by other researchers for Pt SLRR fabrication. Furthermore, a large body of fundamental work has been published on SLRR of Cu.[21,22]

The SLRR process, which relies on the difference in reduction potentials between Cu and Pt to use Cu as a reducing agent for Pt, is traditionally assumed to follow the stoichiometry outlined in eqs 1 and 2 but is currently under investigation to determine if this stoichiometry is accurate.[23,24]

$$Cu^{2+} + 2e^{-} \rightarrow Cu \quad (1)$$

$$Pt^{4+} + 2Cu \rightarrow Pt + 2Cu^{2+} \quad (2)$$

While eqs 1 and 2 outline the most commonly accepted reaction pathway for Pt SLRR, it will be shown here that eq 2 is not always accurate for the reduction of cationic Pt species and that sometimes Pt is deposited in cationic, or oxidized, form. Furthermore, we show in this work that the propensity for cationic Pt formation depends on the number of monolayers of Pt and on the underlying Au morphology.

CFP supports were chosen due to their affordability, high surface area, and efficiency as current collectors for fuel cells. Au nanostructures were electrodeposited on the CFP directly. The direct use of CFP as opposed to graphite coated on CFP leads to improved electrical conductivity and stability.[25] Using CFP, we can also exclude the presence of organic binder agents and other nonconductive materials while efficiently preventing the aggregation of nanoparticles.[8,26] It will be shown that the morphology of the Au−CFP structure as substrate for the ultrathin Pt layers can be well controlled by tuning the deposition parameters. It will also be shown that these changes in the Au morphology are integral to the surface chemical state as measured by X-ray photoelectron spectroscopy (XPS), atomic structure as measured by X-ray absorption fine structure (EXAFS) and X-ray absorption near edge structure (XANES), electrochemical performance, and stability of the ultrathin Pt catalyst.

EXPERIMENTAL SECTION

In all cases, deionized water from a Barnstead NanoPure system (18.2 MΩ) was used. Chemicals were purchased from Sigma-Aldrich and Alfa Aesar. Commercially available CFP was used directly for all substrates. Reference electrodes were Ag/AgCl electrodes, and all potentials are reported relative to Ag/AgCl. Pt wire was used for all auxiliary electrodes. All electrodeposition and galvanic replacement reactions were conducted at room temperature in glass cells. All solutions were deaerated by bubbling with ultrahigh purity dry nitrogen before the chemical processes.

Prior to usage, the CFP electrodes were cleaned by cyclic voltammetry (CV) at 50 mV/S in a 0.5 M H_2SO_4 solution. The Au modification was performed by either PSD at 0 V for 30 minutes or by PSWD alternating between 0 V and 0.6 V in 2.5 mM $AuCl_3$ solution. The resulting Au−CFP structures were cleaned and activated by cycling the

Scheme 1. Representative Schema Demonstrating (a) Metallic Pt Growth on Carbon Paper Containing Large Au Structures and (b) Oxidic Pt Growth on Carbon Paper with Smaller Au Structures

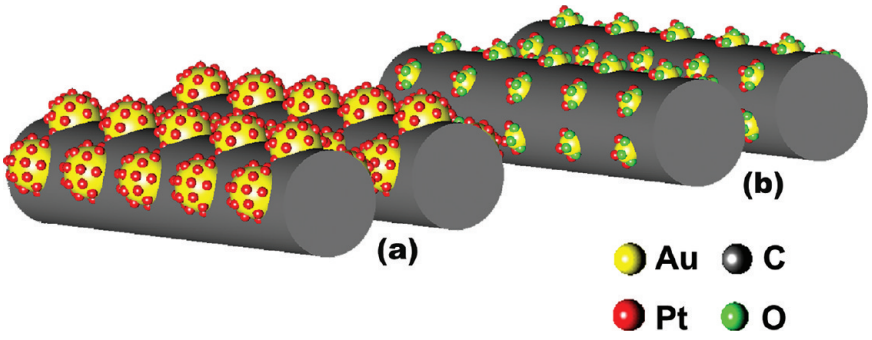

potential between 0 and 1.5 V in 0.5 M H_2SO_4 solution until a stable voltammogram was obtained.

The Cu UPD on Au/CFPs was performed in 50 mM H_2SO_4 containing 10 mM $CuSO_4$. Pt replacement was conducted in deaerated 1 mM H_2PtCl_6 for a minimum of 5 min. Scanning electron microscopy (SEM) was conducted in a Hitachi VP-SEM systerm, while X-ray photoelectron spectroscopy (XPS) was performed in Thermo K-Alpha system. The CV data were collected using a Solartron 1287 potentiostat and a Pine WaveNano potentiostat. EXAFS and XANES data were collected at beamlines X18B and X23A2 at the National Synchrotron Light Source, Brookhaven National Laboratory.

RESULTS AND DISCUSSION

1. Electrode Fabrication. Modification of the CFP electrodes with Au nuclei of varying sizes was conducted by electrodeposition using 30 minutes of either PSD at 0 V or PSWD alternating between 0 V and 0.6 V. The voltage waveforms and current−time transients for the initial time period of both deposition methods can be seen in Figure 1a,b, respectively. It can be seen for the PSD curve that the electrodeposition current drops off markedly in a short period of time. It is worth noting in the PSWD curve that the electrodeposition current is renewed with each current pulse, indicating that the desired effect of replenishing the depletion zone around the electrode was achieved.

After preparation of the Au−CFP electrodes, the resulting Au surfaces were modified by iterative growth of submonolayer coverages of Pt grown via SLRR of Cu UPD films. This modification is illustrated in Scheme 1. The Cu UPD process was conducted by sweep voltammetry in which a bulk deposit of Cu was grown, then stripped, leaving behind only the UPD partial monolayer. A representative voltammogram of the Cu UPD process is shown in Figure 1c, by which the bulk deposition and stripping process can be seen. By stopping the voltage sweep at a potential between the bulk removal and the UPD removal features in the positive-going sweep, the surface coverage of the Cu UPD layer on Au was specified to 0.67 monolayers (ML). This value is obtained from previous STM studies for Cu UPD on pure Au electrodes.[27] The bulk-stripping method has the advantage of providing a cohesive UPD deposit as well as ensuring that no overpotentially deposited Cu remains on the CFP surface.

As a result of the SLRR process, Pt is nominally deposited on the Au surface in a 1:2 Pt/Cu ratio. This ratio arises from the ratio of the valencies of the solvated species (Pt^{4+} and Cu^{2+}). As a result, each iteration of Pt replacing 2/3 ML Cu nominally yields 1/3 ML-equivalent (ML-EQ) of Pt. Thus, one replacement iteration is denoted 0.3 ML-EQ, while 3 growth iterations would be denoted 1 ML-EQ.

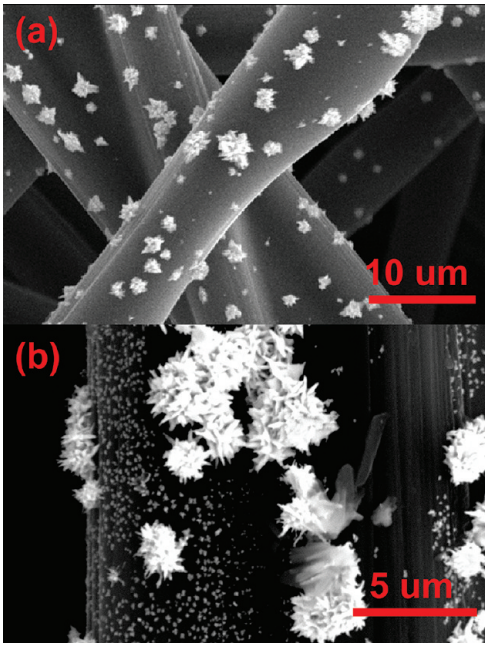

Figure 2. SEM images of the Au−CFP electrodes: (a) PSD at 0 V for 30 min; (b) PSWD for 30 min.

2. Characterization. *a. SEM.* The morphologies of the Au−CFP and Pt−Au−CFP nanostructures were characterized by scanning electron microscopy (SEM). It was found that there is no appreciable difference detectable in SEM imaging between the Au−CFP and Pt−Au−CFP electrodes. This is to be expected due to the extremely small scale of the Pt deposition being conducted. Thus, only the images of Au−CFP prior to Pt deposition are shown in Figure 2. For PSD at 0 V, the Au deposit takes on the morphology of nanoneedles aggregated into large urchin-like clusters with an average diameter of several micrometers (Figure 2a).

It was found that, for the PSWD-grown Au (Figure 2b), there are two types of Au nanostructure coexisting on the CFP surface. First, the urchin-like structures noted earlier are once again present, this time smaller in size. In addition to these larger structures, we see the addition of highly dispersed Au nanoparticles with sizes in the tens of nanometers as a result of the PSWD

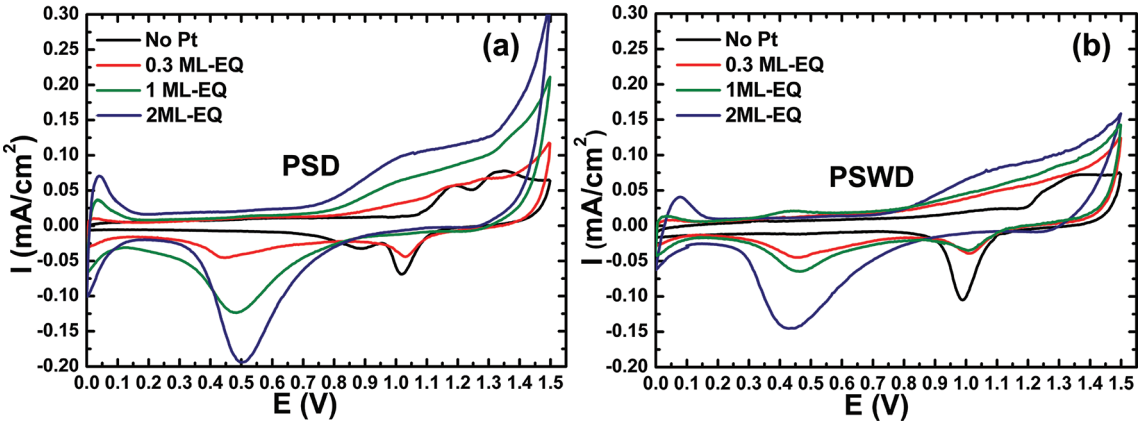

Figure 3. (a) PSD and (b) PSWD: cyclic voltammograms (CVs) of Pt−Au−CFP electrodes in 0.5 M H_2SO_4 solution with a potential scan speed of 20 mV/s.

treatment. These particles are seen to coat the remainder of the exposed CFP. This type of morphological difference between the two growth modes is to be expected based on a simple model for diffusion-limited nucleation and growth. Here, we make the reasonable assumption of diffusion-limited growth (that is, the rate-limiting step for $Au^{3+} \rightarrow Au$ is the arrival of solution-phase Au^{3+} at the CFP surface). During the PSD growth step, a depletion zone of Au^{3+} in the solution is formed after initial Au nuclei formation. Once this zone is formed, the arrival of further Au^{3+} ions to the Au−CFP surface will occur primarily at the nucleated Au nanoneedles, since they protrude into the depletion zone further than the (locally flat) CFP surface. This leads to large needle-like structures extending from initial Au nucleation sites, which also leads to increased electric fields near the surface sites. On the other hand, if we perform a pulsed deposition such as that used for the PSWD samples, we allow this depletion zone to repopulate with solution-phase Au^{3+} during the pulse relaxation, such that new nuclei formation, rather than existing nuclei growth, is the primary reaction during the subsequent voltage pulse.

b. CV. In addition to morphological characterization using SEM, the surface coverage of Pt on the Au deposits was examined by CV in acidic media and comparison of the relative currents associated with Au or Pt surface oxide reduction. Figure 3 shows CV curves for Au−CFP with and without varying coverages of Pt. The CV presented here were recorded in 0.5M H_2SO_4 at 20 mV/s. By examining the decrease in the Au reduction feature at 1.0 V with increased deposition iterations, we can track the amount of Au surface area lost due to masking by Pt deposits. Similarly, increases in Pt surface area can be tracked by studying the Pt oxide reduction feature near 0.47 V or the hydrogen adsorption/desorption curves in the 0 V region of the voltammograms. It can clearly be seen that, with increasing amounts of Pt, the Pt surface area increases at the expense of the Au surface area, indicating that Pt deposition at Au sites is dominant. This method of tracking Pt coverage on Au has been employed successfully in the past.[28,29]

c. X-ray Photoelectron Spectroscopy. XPS analysis was employed to determine the oxidation state of the platinum. The Pt 4f photoemission region for Pt catalysts grown by SLRR on PSD and PSWD Au−CFP is presented in Figure 4a−c, and the results after peak fitting are summarized in Table 1. A representative plot of the peak-fitting performed is shown in Figure 4d, and a comparison of the Pt4f/Au4f ratio (Au4f spectra not shown) is plotted in Figure 4e as a means to track the total Pt content. The Pt4f photoemission exhibits a spin-orbit-split doublet, with two peaks ($4f_{7/2,5/2}$) exhibiting a known spacing of 3.3 eV. In this case, three pairs of peaks were observed in the Pt4f region. This indicated the presence of three types of Pt in differing oxidation states. Each pair of peaks has a similar full-width at half-maximum (FWHM) and a separation of 3.3 eV as expected. The peaks located at 71.19 and 74.49 eV are undoubtedly due to Pt^0, which is found to be the predominant species in most Pt catalysts.[30] The features located at 72.46 and 75.76 eV are due to Pt^{2+}, and the last pair at 74.67 and 77.97 eV originate from Pt^{4+} species.[1,3] The percentage of Pt^0, Pt^{2+}, and Pt^{4+} for Pt on Au−CFP grown by PSD and by PSWD are summarized in Table 1. While the oxidation states for the PSD and PSWD samples are virtually identical for 0.3 ML-EQ of Pt on Au, the Pt^{4+} state disappeared completely after 1 ML-EQ of Pt deposition for the PSD-grown Au−CFP supports. In comparison, some Pt^{4+} species remained present in the film for all iteration numbers of Pt on PSWD-grown Au−CFP.

Even though the percentages of Pt^{4+} decrease along with the Pt thickness for both sets of samples, the rate of this decrease is much lower for the PSWD series than for the PSD series. Although the optimum ratio of these three states is unclear, it is clear from the literature that the existence of Pt oxides in catalysis plays a significant role in performance.[9,26] Thus, it is of critical importance that the influence of support particle size be considered when growing ultrathin noble metal deposits for application. On the basis of the evidence for cationic Pt formation, we present here an alternate reaction pathway to eq 2.

$$Pt^{4+} + 2Cu + L^- \rightarrow xPt + y[Pt^{2+}(2/\delta)L^{-\delta}] + (1-x-y)[Pt^{4+}(4/\delta)L^{-\delta}] + (2-y)Cu^{2+} \quad (3)$$

eq 3 indicates the coexistence Pt^0, Pt^{4+}, and Pt^{2+} species on the surface, coordinated with an as-yet unidenfitied anionic ligand $L^{-\delta}$. We will see in later sections that the use of EXAFS analysis allows us to tentatively identify this complexing ligand species based on interatomic bond lengths measured for the cationic Pt. The determination of a new reaction mechanism for the growth of SLRR layers is not unheard of; in fact, a recent study by Brankovic et al. has shown that anionic species such as Cl^- may act as complexing agents with the dissolving Cu, resulting in only partial oxidation of the Cu adlayer leading to

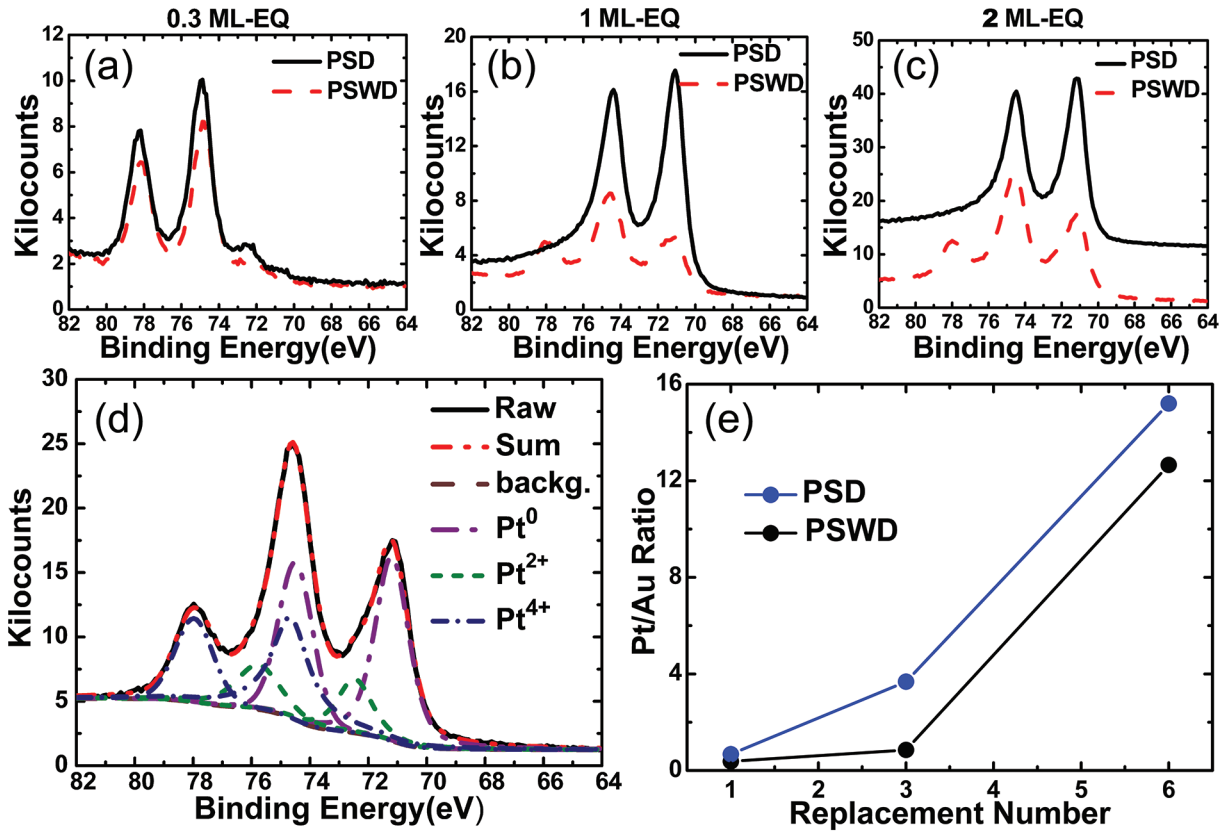

Figure 4. Pt4f XPS for Pt−SLRR on Au−CFP grown by PSD and PSWD. (a) 0.3 ML-EQ, (b) 1 ML-EQ, (c) 2 ML-EQ. (d) Representative peak-fitting of the PSWD 2 ML-EQ curve. (e) Plot of the Pt/Au peak ratios resulting from peak-fitting of Pt and Au 4f features.

Table 1. Binding Energy (BE) and Relative Intensities for Pt 4f Photoemissions[a]

			peak area percentage					
	binding energy (eV)		PSD			PSWD		
Pt species	$4f_{7/2}$	$4f_{5/2}$	0.3 ML-EQ	1 ML-EQ	2 ML-EQ	0.3 ML-EQ	1 ML-EQ	2 ML-EQ
Pt^0	71.19	74.49	10.2	65.7	65.1	9.8	55	48.7
Pt^{2+}	72.46	75.76	14.5	34.3	34.9	15.3	15.6	17.9
Pt^{4+}	74.67	77.97	75.3	0	0	74.9	29.4	33.4

[a] Estimated error in peak-fitted areas is +/− 5%. The resolution for binding energy measurements here is estimated to be 0.3 eV.

a 1:4 Pt/Cu replacement ratio.[22] While the previous work by Brankovic et al. focused on the effects of complexing anionic species interacting with the dissolving UPD layer, it is apparent from the XPS data presented here that these anionic species may also incorporate themselves into the deposited Pt layer leading to incomplete reduction of the Pt species. The possibility of co-existence of the effect reported here in addition to the effect reported by Brankovic merits further investigation, but a direct comparison between the two studies cannot be made at this moment due to slight differences in bath composition and growth protocols.

A possible explanation of the Pt oxidation state change, whereby this effect was caused by partial oxidation of the Au particles grown by the PSWD method, was disproved by XPS analysis of the Au 4f photoemission (not shown), which indicated that the Au deposits were metallic. This leaves two alternative effects that could be responsible for this phenomenon, the existence of a size-dependent effect in the Pt−Cu replacement reaction and/or the influence of Au−CFP boundary sites on the Pt^{4+} reduction reaction. The fact that the 0.3 ML-EQ deposits are virtually identical for both series of samples seems to suggest that the size effect is more likely, as the difference in size would only become an issue once near-full coverage of Pt on Au was reached.

In addition to quantifying the portion of Pt present by valence state, it was possible to quantify the overall amount of Pt present on the surface relative to the Au support. By analyzing the peak area ratios of the Pt_{4f} and Au_{4f} photoemissions, a relative quantification of the Pt deposit can be achieved. These peak area ratios are shown as a function of Pt coverage in Figure 4e.

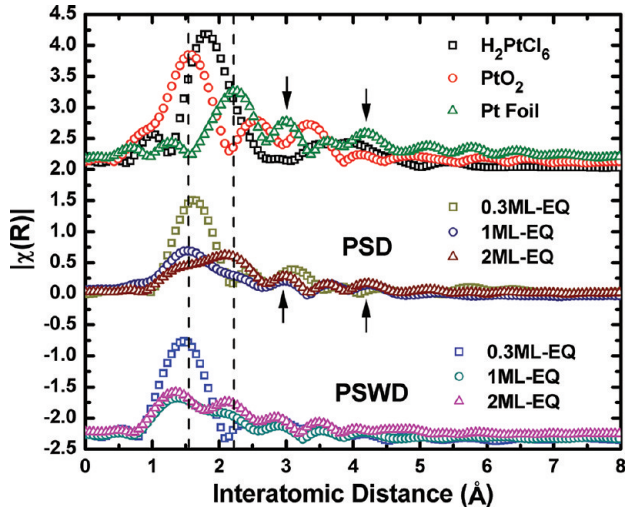

Figure 5. EXAFS spectra for reference compounds, PSD, and PSWD samples. Vertical lines mark the location of first-neighbors for reference PtO_2 and PtCl, and arrows mark the location of common features between the metal foil reference and the metallic components of the Pt films.

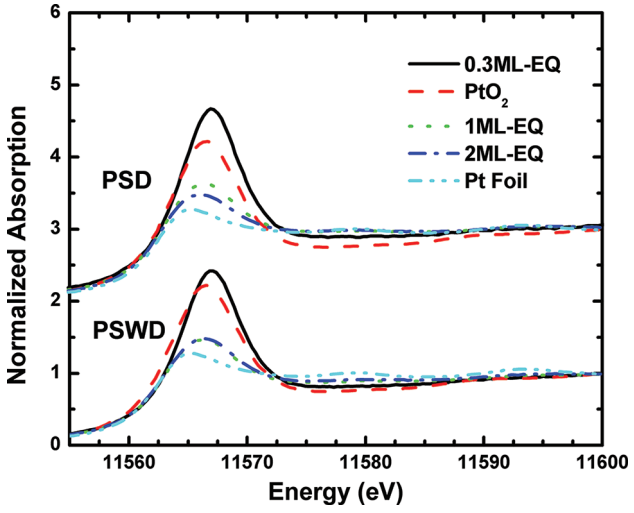

Figure 6. XANES spectra for the SLRR-fabricated samples and reference compounds. Reference spectra are shown for both PSD and PSWD series.

For both groups of catalysts, the relative intensity of Pt compared to Au increases along with increasing replacement iterations, as expected.

d. X-ray Absorption Measurements. In order to better understand the phenomenon of cationic Pt formation, EXAFS and XANES studies of the Pt−Au−CFP electrodes were conducted to investigate the local atomic structure and d-band occupancy of the Pt film, respectively. Figure 5 presents the EXAFS data for both the PSD and PSWD series of samples along with reference data, while Figure 6 presents the XANES data.

In Figure 5, we see the r-space spectra, which are proportional to the radial distribution function around an average Pt atom. The EXAFS data allow us to analyze the immediate atomic vicinity of the Pt atoms within the Pt film. By comparison of the location of the first peak with the reference spectra, we can begin to identify the type of bonding present around the average Pt atom. It is clear from examination of the reference spectra that Pt−Pt metallic bonding exhibits a peak near 2.2 Å, while the Pt−Cl and Pt−O bonds show significantly shorter bond lengths (1.9 Å and 1.7 Å, respectively). It is important to note that backscattering phase shifts have not been corrected for this analysis in either the sample spectra or the reference spectra. This allows for meaningful comparison between the reference and sample, although exact determination of bond length is not achieved. It is clear that the 0.3 ML-EQ curves for both sets of samples in Figure 5 exhibits bond lengths characteristic of Pt−O, with a first coordination shell at 1.7 Å lining up nearly exactly with the reference spectra for PtO_2. We see a small shift in the location of the first coordination shell for 0.3 ML-EQ on PSD compared with 0.3 ML-EQ on PSWD, which suggests that the Pt−O surface lattice exhibits some small amount of strain-induced distortion.

When examining the 1 ML-EQ and 2 ML-EQ films in Figure 5, we see that each film exhibits two coexisting components of the first neighbor shell; one located at 1.7 Å, and one located at 2.2 Å. This holds true for both the PSD and PSWD series of curves and indicates a mixed oxide-metallic structure, with the addition of metallic species upon increased deposition iterations appearing as increased intensity at 2.2 Å. It is worth noting that by the time 2 ML-EQ of Pt on PSD-grown Au−CFP has been reached, the metallic Pt−Pt contribution at 2.2 Å is noticeably larger than the Pt−O at 1.7 Å. In contrast to this, the Pt−Pt contribution for the same 2 ML-EQ PSWD sample is significantly weaker than its corresponding Pt−O contribution. This confirms the finding in XPS that indicated that the PSWD samples had increased oxide content compared to the PSD samples. Furthermore, we are able to tentatively identify the complexing ligand for the cationic Pt surface oxides as oxygen based on these bond lengths. Thus, it is possible to revise eq 3:

$$3Pt^{4+}_{(aq)} + 3Cu_{(ads)} + 3O^{2-}_{(aq)} \rightarrow Pt_{(ads)} + PtO_2(IV)_{(ads)} + PtO(II)_{(ads)} + 3Cu^{2+}_{(aq)} \quad (4)$$

Note that eq 4 still indicates the presence of Pt of all three valencies observed in XPS and that the ratio of the two species is difficult to determine using EXAFS data. One final point to address in the EXAFS data analysis is the question of why the metal/oxide ratio appears higher in XPS than in EXAFS. This discrepancy results from the ordering dependence of the r-space EXAFS data. While XPS is only sensitive to the chemical bonding and the raw amounts of a given Pt species, EXAFS features will become more intense as a given phase increases in local ordering. Since we observe higher ratios of cationic species to metallic species in EXAFS than we do in XPS, we can conclude that the cationic/oxidic phases formed by the Pt SLRR process are more ordered than the metallic phases.

In the XANES spectra in Figure 6, we see a series of plots for reference spectra and Pt SLRR on PSD and PSWD samples. By tracking the intensity of the white line absorption, which is proportional to the density of unoccupied d-band states in the material, we find another marker for the oxidic character of the Pt film. Since oxides tend to display more intense white line resonances (because of the d-state holes), we expect the thinner Pt deposits to exhibit large peaks in R than the thicker Pt deposits. This trend is found to hold true exactly for the PSD series of samples, with each successive increase in Pt deposit thickness leading to a further decrease in XANES white-line

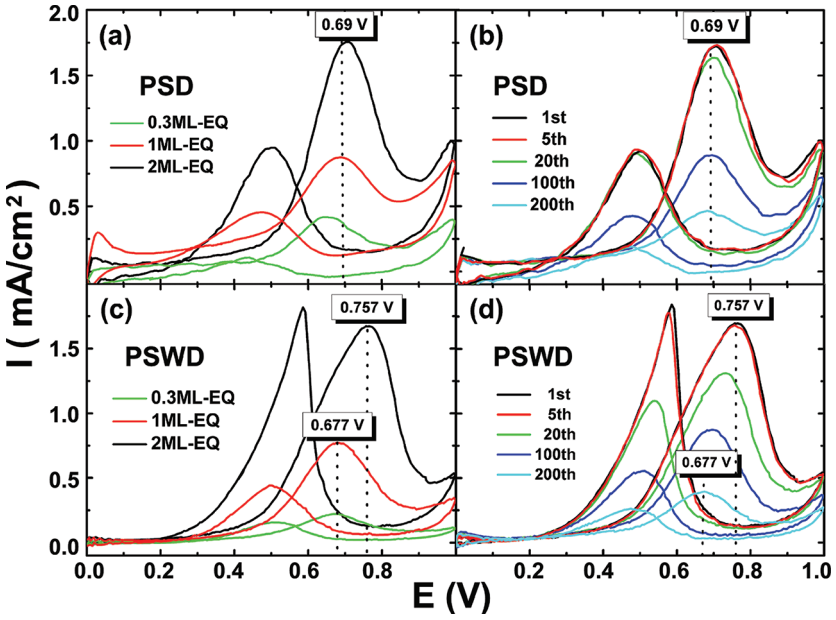

Figure 7. CV in 0.5M H_2SO_4 + 0.5M CH_3OH at 50 mV/s for Pt SLRR grown on Au−CFP electrodes. (a) First cycle voltammetry for PSD samples and (b) durability over multiple cycles for 2 ML-EQ Pt on PSD-grown Au−CFP. (c) First cycle voltammetry for PSWD samples and (d) durability over multiple cycles for 2 ML-EQ Pt on PSWD-grown Au−CFP.

intensity. However, if we examine the PSWD series of samples, we see that while the 1 ML-EQ sample shows a weaker white-line intensity than the 0.3 ML-EQ sample (indicative of reduced cationic content); the 2 ML-EQ sample is virtually identical to the 1 ML-EQ sample. This observation serves as a third independent confirmation of the result initially found in XPS: that the PSWD series of samples exhibits a marked increase in cationic Pt content compared to the PSD series of samples, particularly for Pt deposits of 2 ML-EQ.

A second important observation of the XANES spectra is found by comparison of the PSD 0.3 ML-EQ curve with the PSWD 0.3 ML-EQ curve. Compared to the PtO_2 reference, which is the same in both sets of spectra, the PSD 0.3 ML-EQ sample exhibits a more intense white line than the PSWD sample of similar coverage. This difference suggests that some degree of electron donation from the PSWD Au substrate is leading to decreased d-band vacancies in the Pt film. This is congruent with the smaller deposits arising from the PSWD fabrication process, which should exhibit a higher degree of Au−Pt interaction due to their higher Au surface/volume ratios compared to the PSD deposits.

3. Methanol Electro-oxidation. In order to test the electrocatalytic activity of the electrodes for MOR, samples were cycled from 0 to 1.0 V up to 300 times in 0.5M CH_3OH + 0.5M H_2SO_4. This data is presented in Figure 7, with plots a and c showing maximum peak currents for different SLRR treatments of the PSD and PSWD-grown Au−CFP electrodes, respectively. Plots b and d of Figure 7 show the decay in methanol oxidation current over multiple cycles, in both cases for 2 ML-EQ of Pt on PSD and PSWD samples, respectively. This type of multi-cycle oxidation test allows for relatively simple characterization of catalyst deactivation processes arising from poisoning or Pt dissolution. By tracking the peak oxidation current for any given cycle, a measure of the remaining electrochemically active Pt surface area can be obtained. Since Au does not appreciably catalyze the MOR compared to Pt, the entire oxidation current (and corresponding decreases in that current) can be ascribed to Pt sites. At the same time, since the MOR does not provide a method for testing for re-exposure of Au sites, it is difficult to determine whether the decreases in Pt oxidation current presented here arise from poisoning, agglomeration, or corrosion effects. Even though this determination cannot be performed exactly, we suggest that the majority of Pt current loss is due to Pt agglomeration and removal effects, since the surface poisons created during methanol electro-oxidation should be desorbed during the low-potential segment of each oxidation cycle.

All Pt−Au−CFP electrodes exhibited some degree of cleaning phase at the beginning of MOR cycling, during which the peak currents increased until reaching a maximum before decreasing once again. These cleaning stages are omitted from the plots here, with the initial cycle being ascribed to the maximum oxidation current observed. Increases in methanol oxidation currents are apparent from 0.3 ML-EQ coverage to 2 ML-EQ coverage in both groups of catalysts. The peak currents of the 1 ML-EQ (3 iterations) and 2 ML-EQ (6 iterations) catalysts are 3 and 6 times as high as the 0.3 ML-EQ (1 iteration) catalyst, respectively. This indicates that the thicker deposits (which exhibited more metallic-type behavior in XPS and X-ray absorption spectroscopy (XAS)) are in all cases more active for the MOR than the thinner deposits. While some portion of the effect may be attributable to increases in total Pt surface area, the oxidation state of the Pt film also make a definite contribution to the activity towards the MOR. This contribution can be seen by comparing maximum currents exhibited in Figure 7a with those in Figure 7c. It is apparent from direct comparison that the PSD-grown Au support leads to higher MOR currents than the PSWD-grown support. In the absence of any concerns regarding cationic Pt, one would expect the nanostructured architecture arising from PSWD growth to exhibit larger surface area than the micrometer-scale architecture arising from PSD growth. Thus, we can attribute the decrease in activity shown by the PSWD samples to the increased cationicity already observed in XPS and XAS.

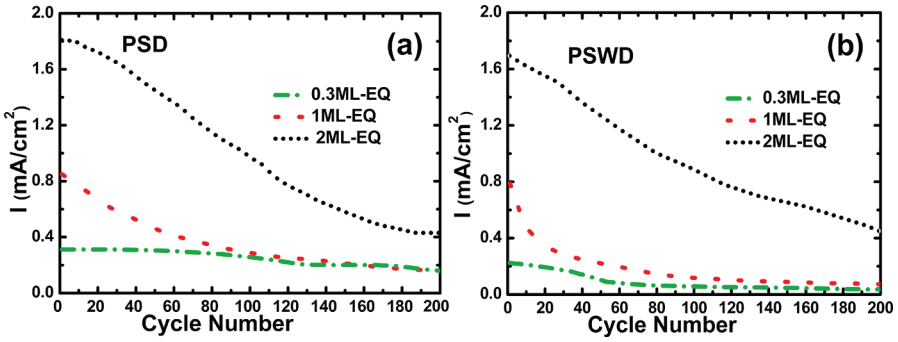

Figure 8. Peak current histogram for the methanol electro-oxidation reaction on all 6 Pt−Au−CFP electrode surfaces studied.

The authors have extrapolated the mass activity of Pt (in terms of peak oxidation current per unit mass) by calculating the nominal Pt mass based on a 1:2 Pt/Cu replacement ratio and the measured Au surface areas. We find that mass activities (taken as methanol peak current per unit Pt mass) for 1 ML-EQ Pt deposits are 2 mA μg^{-1} for the PSD case and 1.75 mA μg^{-1} for the PSWD case. These values lie within the realm of acceptability when compared to other well-cited studies.[31] It should be noted, however, that XPS and XAS results presented in this work indicate that the 1:2 replacement ratio is good as a first order approximation but, in fact, the actual replacement reactions deviate slightly from this ratio.

Further evidence for the detrimental effect of cationic Pt on the MOR is apparent in Figure 7c,d, in which a positive potential shift for the peak current of the MOR at early cycles of 2 ML-EQ Pt can be seen. This type of shift is only seen for PSWD samples and not for PSD samples, indicating that the decreased size of the Au support particles (and the corresponding increase in cationic Pt) is correlated with this positive shift. It has already been shown that lower reaction potentials for the MOR are indicative of a more active Pt catalyst. Thus, it is clear that the positive shift in peak potential arises from a detrimental accumulation of cationic Pt, leading to deactivation of the catalyst surface. It is important to remember from the quantitative XPS analysis that, even though the proportion of cationic Pt remains roughly equal between 1 ML-EQ and 2 ML-EQ of Pt on the PSWD samples, the overall platinum content is increasing, leading to large quantities of cationic Pt in the 2 ML-EQ film relative to the 1 ML-EQ or 0.3 ML-EQ films. In Figure 7d, we see that, as the Pt loses active surface area, this positive shift is eventually eliminated, with the MOR curve after 20 reaction cycles having shifted to a potential more characteristic of the other Pt electrode surfaces.

In addition to the potential of maximum current and the total electro-oxidation peak current itself, the long-term stability of an ultrathin Pt film is a very important property for this type of fuel cell electrocatalyst. Even though voltammograms for all coverages of Pt on Au−CFP were collected, it is not practical to attempt to plot all of the voltammograms, so only the long-term stability results of 2 ML-EQ Pt on PSD and PSWD Au−CFP are presented in Figure 7b,d. We see here clearly that the peak current obtained from the forward CV scans gradually decreases along with the successive CV scans. We can see clearly that for the 2 ML-EQ PSWD sample in Figure 7d after 200 CV scans, the peak current density is 1.2 mA·cm^{-2}, which is 40% of the value of the peak current density at first cycle (3.0 mA·cm^{-2}). The decrease of the peak current density could result either from Pt degradation by agglomeration/corrosion processes or from the poisoning of the catalyst by the intermediates (such as (CO) adsorption) of methanol oxidation.[2,29] It is also worth noting that the peak current for the PSWD catalyst (Figure 7d) decays significantly more quickly than for the PSD catalyst (Figure 7b) in the first 20 cycles. This increased rate of decay corresponds with a return to lower MOR electro-oxidation potentials and suggests that the cationic Pt is quickly attacked and compromised during the initial cycles of MOR reaction.

The MOR peak current histogram as a function of cycle number for the remaining coverages studied (0.3 ML-EQ through 2 ML-EQ on both PSD and PSWD) is plotted in Figure 8. From this data, we can clearly see that, after about 100 cycles, there is almost no remaining electro-oxidation current for 0.3 ML-EQ and 1 ML-EQ on both PSD and PSWD, which indicates that the Pt deposit has been mostly deactivated through either dissolution or poisoning. Additionally, the peak currents decay faster during the first 20 cycles for PSWD deposits than for the PSD deposits. It is possible that we witness easier deactivation of the PSWD sample due to the higher degree cationicity of the Pt deposit as proven in the above text. It is also possible that the smaller particles size of the Au substrate induced faster coalescence of the Au particles themselves, leading to decreased Pt surface area.[32]

Thus, we can conclude that the propensity to form cationic Pt as shown via XPS and XAS analysis is detrimental to the performance of the Pt/Au−CFP electrodes for monolayer and submonolayer coverages, leading to decreased activity and durability. However, for 2 ML-EQ, both the PSD and PSWD morphologies exhibit comparable MOR durability histograms, indicating that, for Pt deposits of a minimum 2 ML-EQ thickness, these detrimental effects can be eliminated. In summary, we have identified a low-loading thickness limit of 2 ML-EQ, below which the Pt film exhibits decreased activity and durability due specifically to chemical and structural changes arising from the morphology of the Au support. The authors suggest that factors such as increased defect concentration or nonequilibrium structure of the PSWD-grown Au support may be responsible for the changes in Pt behavior observed. These possibilities are supported by the XAS data which indicates that the monolayer-scale Pt does not effectively arrange itself in FCC structure on PSWD deposits. It is also supported by XPS data which indicates that partial oxidation of the smaller Au deposits is not the cause of these effects. Above the 2 ML-EQ limit, the Pt film may still behave differently than a bulk Pt structure, but the morphology of the Au support loses much of its influence on the Pt film behavior. These findings are of particular importance for the

subset of the fuel-cell catalyst community that is focused on core-shell or layered structures, indicating that morphology-related support effects may lead to pronounced detrimental effects if a minimum amount of Pt is not achieved.

CONCLUSIONS

Controlled monolayer-scale Pt deposits were fabricated on two kinds of Au structures with differing size scales. These deposits were fabricated on carbon fiber paper electrodes through electrochemical deposition processes by manipulating the deposition potential. A series of corresponding Pt−Au−CFP catalysts on both Au morphologies was prepared by Cu UPD and subsequent redox replacement of Pt^{4+} ions. In addition to metallic Pt, cationic Pt species including Pt^{2+} and Pt^{4+} were detected in XPS and EXAFS spectra. A trend is reported by which increasing iterations of the SLRR growth process of Pt lead to a more metallic surface chemistry and atomic structure in the Pt catalyst surfaces. Furthermore, it was found that the use of Au nanoparticles on CFP as a support caused this cationic Pt species to be present at higher iteration numbers, while the larger Au morphologies showed a faster trend towards metallic deposits. Thus, it is reported that the valency of SLRR-grown Pt shows a strong dependency on the size of the Au particles on which it is performed.

Finally, the Pt−Au−CFP surfaces were tested for performance and durability under oxidation cycling in the methanol−acid system. It was found that the Pt deposits grown on larger Au supports exhibited markedly improved durability during the first 20 electro-oxidation cycles and slight improvements in activity compared to the nanoparticle Au supports. This leads us to conclude that the cationic Pt species induced by the smaller-scale Au supports is less active towards the methanol electro-oxidation reaction as well as less durable than metallic-type Pt species shown to grow on larger-scale Au supports. Finally, it has been shown that an equivalent of two monolayers is the low-loading limit of Pt on Au below which the Pt film decreases in activity and durability very rapidly due to presence of cationic Pt in that dimensional domain.

AUTHOR INFORMATION

Corresponding Author

*E-mail: faisal.alamgir@mse.gatech.edu.

ACKNOWLEDGMENT

The authors acknowledge technical support from Dr. Bruce Ravel at beamline X23A2 and beamline staff at X18B of the NSLS. We also acknowledge the Synchrotron Catalysis Consortium for travel support to the NSLS. We also would like to thank the Department of Energy, grant number DE-FG02-97ER14799, for the support of this work. Funding support from the Petroleum Research Fund of the American Chemical Society is acknowledged. S.C. wishes to thank the China Scholarship Council for the fellowship support.

REFERENCES

(1) Selvarani, G.; Selvaganesh, S. V.; Krishnamurthy, S.; Kiruthika, G. V. M.; Sridhar, P.; Pitchumani, S.; Shukla, A. K. *J. Phys. Chem. C* **2009**, *113*, 7461.

(2) Ge, X.; Wang, R.; Liu, P.; Ding, Y. *Chem. Mater.* **2007**, *19*, 5827.

(3) Goodenough, J. B.; Hamnett, A.; Kennedy, B. J.; Manoharan, R.; Weeks, S. A. *J. Electroanal. Chem.* **1988**, *240*, 133.

(4) Martin, S.; Garcia-Ybarra, P. L.; Castillo, J. L. *Int. J. Hydrogen Energy* **2010**, *35*, 10446.

(5) Mougenot, M.; Caillard, A.; Brault, P.; Baranton, S.; Coutanceau, C. *Int. J. Hydrogen Energy*, in press.

(6) Tsiouvaras, N.; Peña, M. A.; Fierro, J. L. G.; Pastor, E.; Martínez-Huerta, M. V. *Catal. Today* **2010**, *158*, 12.

(7) Alcaide, F.; Álvarez, G.; Cabot, P. L.; Miguel, O.; Querejeta, A. *Int. J. Hydrogen Energy* **2010**, *35*, 11634.

(8) Onoe, T.; Iwamoto, S.; Inoue, M. *Catal. Commun.* **2007**, *8*, 701.

(9) Rettew, R. E.; Guthrie, J. W.; Alamgir, F. M. *J. Electrochem. Soc.* **2009**, *156*, D513.

(10) Podlovchenko, B.; Gladysheva, T.; Filatov, A.; Yashina, L. *Russ. J. Electrochem.* **2010**, *46*, 1189.

(11) Li, X. W.; Liu, J. Y.; Huang, Q. H.; Vogel, W.; Akins, D. L.; Yang, H. *Electrochim. Acta* **2010**, *56*, 278.

(12) Gavrilov, A. N.; Petrii, O. A.; Mukovnin, A. A.; Smirnova, N. V.; Levchenko, T. V.; Tsirlina, G. A. *Electrochim. Acta* **2007**, *52*, 2775.

(13) Zhao, D.; Wang, Y.-H.; Xu, B.-Q. *J. Phys. Chem. C* **2009**, *113*, 20903.

(14) Zhao, D.; Xu, B. Q. *Angew. Chem., Int. Ed.* **2006**, *45*, 4955.

(15) Cao, L.; Tong, L.; Diao, P.; Zhu, T.; Liu, Z. *Chem. Mater.* **2004**, *16*, 3239.

(16) Luo, J.; Maye, M. M.; Petkov, V.; Kariuki, N. N.; Wang, L.; Njoki, P.; Mott, D.; Lin, Y.; Zhong, C.-J. *Chem. Mater.* **2005**, *17*, 3086.

(17) Zhang, J.; Sasaki, K.; Sutter, E.; Adzic, R. R. *Science* **2007**, *315*, 220.

(18) Park, I.-S.; Lee, K.-S.; Jung, D.-S.; Park, H.-Y.; Sung, Y.-E. *Electrochim. Acta* **2007**, *52*, 5599.

(19) Zhang, G.; Kuang, Y.; Liu, J.; Cui, Y.; Chen, J.; Zhou, H. *Electrochem. Commun.* **2010**, *12*, 1233.

(20) Fayette, M.; Liu, Y.; Bertrand, D.; Nutariya, J.; Vasiljevic, N.; Dimitrov, N. *Langmuir* **2011**, *27*, 5650.

(21) Mrozek, M. F.; Xie, Y.; Weaver, M. J. *Anal. Chem.* **2001**, *73*, 5953.

(22) Gokcen, D.; Bae, S.-E.; Brankovic, S. R. *J. Electrochem. Soc* **2010**, *157*, D582.

(23) Rettew, R. E.; Allam, N. K.; Alamgir, F. M. *ACS Appl. Mater. Interfaces* **2011**, *3*, 147.

(24) Gokcen, D.; Bae, S. E.; Brankovic, S. R. *J. Electrochem. Soc.* **2010**, *157*, D582.

(25) Khosravi, M.; Amini, M. K. *Int. J. Hydrogen Energy* **2010**, *35*, 10527.

(26) Sen, S.; Sen, F.; Gokagac, G. *Phys. Chem. Chem. Phys.* **2011**, *13*, 6784.

(27) Magnussen, O. M.; Hotlos, J.; Nichols, R. J.; Kolb, D. M.; Behm, R. J. *Phys. Rev. Lett.* **1990**, *64*, 2929.

(28) Zhai, J.; Huang, M.; Dong, S. *Electroanalysis* **2007**, *19*, 506.

(29) Tang, H.; Chen, J. H.; Wang, M. Y.; Nie, L. H.; Kuang, Y. F.; Yao, S. Z. *Appl. Catal., A* **2004**, *275*, 43.

(30) Zubrägel, C.; Deuper, C.; Schneider, F.; Neumann, M.; Grunze, M.; Schertel, A.; Wöll, C. *Chem. Phys. Lett.* **1995**, *238*, 308.

(31) Adzic, R.; Zhang, J.; Sasaki, K.; Vukmirovic, M.; Shao, M.; Wang, J.; Nilekar, A.; Mavrikakis, M.; Valerio, J.; Uribe, F. *Top. Catal.* **2007**, *46*, 249.

(32) Xia, Y.; Xiong, Y.; Lim, B.; Skrabalak, S. E. *Angew. Chem., Int. Ed.* **2009**, *48*, 60.